Nanoscale

ROYAL SOCIETY
OF CHEMISTRY

PAPER

View Article Online
View Journal | View Issue

Cite this: *Nanoscale*, 2022, **14**, 3801

A biphenylene nanoribbon-based 3D metallic and ductile carbon allotrope

Wei Sun, Yiheng Shen, Dongyuan Ni and Qian Wang *

Received 21st December 2021,
Accepted 3rd February 2022

DOI: 10.1039/d1nr08384h

rsc.li/nanoscale

Assembling two-dimensional (2D) sheets for three-dimensional (3D) functional materials is of current interest. Motivated by the recent experimental synthesis of 2D biphenylene [*Science* **372** (2021) 852], we propose a new porous 3D metallic carbon structure, named T48-carbon, by using biphenylene nanoribbons as the building block. Based on state-of-the-art theoretical calculations, we find that T48-carbon is not only dynamically, thermally, and mechanically stable, but also energetically more favorable as compared with some other theoretically predicted carbon allotropes. Especially, T48-carbon exhibits mechanical anisotropy, ductility and intrinsic metallicity. A detailed analysis of electronic properties reveals that the metallicity mainly comes from the p_z-orbital of sp^2-hybridized carbon atoms. This work shows the promise of design and synthesis of 3D biphenylene-based metallic carbon materials with novel properties.

1. Introduction

Design and synthesis of 3D metallic carbon that is stable under ambient thermodynamic conditions is a long-term and unremitting pursuit of scientists. Metallic carbon has a high density of states (DOS) at the Fermi level, it can be more effective in catalysis and reaction, can exhibit phonon–plasmon couplings, and can display negative differential resistance (NDR), superconductivity and magnetism when satisfying the Stoner-like criterion.[1] In recent years, it has attracted increasing attention to design 3D metallic carbon allotropes using various carbon nanoribbons as the building blocks. For instance, Liu *et al.*[2] designed a 3D porous metallic carbon allotrope with graphene nanoribbons that exhibits a large phonon heat capacity, high Debye stiffness, anisotropic elasticity and superhardness, and is a promising anode material for Li-ion batteries; Ni *et al.*[3] predicted a 3D metallic carbon, Hex-C_{558}, which is composed of 5-5-8 carbon nanoribbons observed in graphene sheets. Very recently, Li *et al.*[4] proposed a new 3D porous metallic carbon allotrope consisted of penta-graphene nanoribbons, named penta-oC36, and found that penta-oC36 is a promising anode material of sodium-ion batteries with good performance because of its metallicity with regularly distributed conducting channels and low mass density. These research advances clearly show that 2D carbon sheets provide us with an effective platform to design 3D metallic carbon allotropes.

Recently, 2D biphenylene is experimentally synthesized based on an on-surface interpolymer dehydrofluorination reaction.[5] Karaush *et al.*[6] proposed this graphene allotrope consisting of 4-, 6-, and 8-membered carbon rings and predicted it to be stable in 2014. Biphenylene sheets have many novel properties, including a metallic band with an n-type Dirac cone,[7] metallicity of nanotubes regardless of the chiral vector,[8] and strong visible absorption.[9] Furthermore, Ma *et al.*[10] found flat bands in a twisted bilayer biphenylene, and Ferguson *et al.*[11] designed a biphenylene membrane as an anode material for lithium-ion batteries. Following the above ideas, it is natural and interesting to explore whether we can also design a stable 3D metallic carbon allotrope by using biphenylene nanoribbons as the building block.

In this work, by assembling biphenylene nanoribbons, we construct a new 3D carbon monolith named T48-carbon. Different from the recently proposed Tet-C_{52} [12] consisting of biphenylene nanoribbons and zigzag (4,0) nanotubes, T48-carbon is purely composed of biphenylene nanoribbons with the advantages of the simplicity and feasibility of design and synthesis. Based on state-of-the-art theoretical calculations, we find that T48-carbon is stable, and energetically comparable with T6-carbon[1] and even more preferable over some other theoretically predicted carbon allotropes. Moreover, T48-carbon is metallic and exhibits mechanical anisotropy and ductile feature with a relatively high specific heat capacity.

CAPT, School of Materials Science and Engineering, HEDPS, BKL-MEMD, Peking University, Beijing 100871, China. E-mail: qianwang2@pku.edu.cn

2. Computational methods

Our calculations are based on density functional theory as implemented in the Vienna *ab initio* simulation package (VASP).[13] The valence electron wave functions of C ($2s^22p^2$) are expanded by using the projector augmented wave method[14,15] with a kinetic energy cutoff of 600 eV. We used the generalized gradient approximation[16] with the Perdew–Burke–Ernzerhof (PBE) functional for the electronic exchange–correlation, and used the hybrid Heyd–Scuseria–Ernzerhof (HSE06) functional[17,18] for more accurate electronic structures. The first Brillouin zone is sampled with a 6 × 6 × 12 *k*-point grid in the Monkhorst–Pack scheme.[19] To optimize the lattice constants and the atomic configurations, we used the conjugate gradient algorithm with the convergence thresholds of 10^{-8} eV and 10^{-6} eV Å^{-1} for total energy and Hellmann–Feynman force components, respectively. Phonon dispersion is calculated to check the dynamical stability by the finite displacement method[20] as implemented in the Phonopy code.[21] *Ab initio* molecular dynamics (AIMD)[22] simulations with the Nosé–Hoover thermostat[23] are performed using a 2 × 2 × 3 supercell to determine the thermal stability.

3. Results and discussion

3.1 Geometric structure

This new carbon monolith is constructed by using biphenylene nanoribbons as the building block with periodically arranged four- and eight-menbered rings as cross-linkers. The schematic diagram, as shown in Fig. 1(a), illustrates the process of constructing a 3D structure from biphenylene nanoribbons. It is encouraging to note that many graphene-based 3D porous structures have been successfully synthesized,[24,25] which would inspire the experimental synthesis of biphenylene-based 3D porous materials. The optimized geometry is plotted in Fig. 1(b). It belongs to a tetragonal crystal system, and contains 48 carbon atoms in a unit cell, thus is named T48-carbon, with a high symmetric space group of *P*4/*mmm* (D4H-1, no. 123) and the lattice constants of $a = b = 9.97$ Å and $c = 4.49$ Å. In this structure, there are three chemically nonequivalent Wyckoff positions, namely, $16u_1$ (0.307, 0.581, and 0.824), $16u_2$ (0.182, 0.628, and 0.658) and $16u_3$ (0.074, 0.658, and 0.838), colored in red, orange and pink, respectively, as shown in Fig. 1(b). For convenience, we name them as C_1, C_2 and C_3, respectively. C_1 atoms form four bonds while other two kinds of carbon atoms only form three bonds, resulting in the overall ratio of 1 : 2 for four- to three-fold coordinated carbon atoms. Due to its porous structure, T48-carbon's calculated equilibrium mass density is just 2.15 g cm^{-3}, which is much lower than that of diamond (3.49 g cm^{-3}).[26]

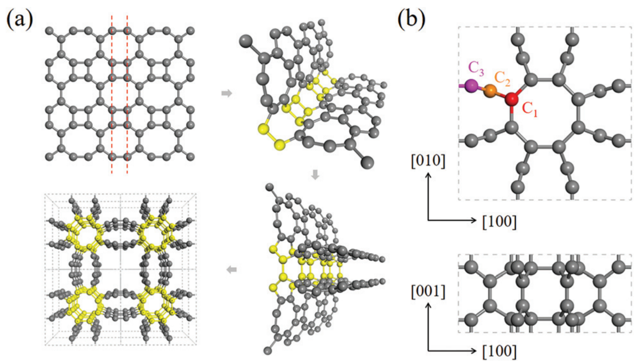

Fig. 1 (a) Schematic of T48-carbon using biphenylene nanoribbons as the building block. (b) An optimized unit cell of T48-carbon. Three colors correspond to representative C atoms occupying different chemically nonequivalent Wyckoff positions.

The dynamic stability of T48-carbon is examined by calculating the phonon spectrum as shown in Fig. 2(b). All the vibrational modes have real frequencies in the entire first Brillouin zone, confirming that T48-carbon is dynamically stable. To check the thermal stability, we performed AIMD simulations at temperatures of 300, 700 and 1000 K for 10 ps with a time step of 1 fs for each simulation. A 2 × 2 × 3 supercell is used to avoid the fake stability resulted from the periodic boundary conditions. Fig. 2(c) shows the result at 1000 K that the geometry of T48-carbon remains nearly intact at the end of the simulation and the total potential energy remains almost invariant. This suggests that T48-carbon can be thermally stable even at 1000 K. To investigate the mechanical stability, we used the finite distortion method[27] to calculate the elastic tensor. According to the tetragonal crystal system of T48-carbon, there are only six independent nonzero components. Their values are $C_{11} = 301$ GPa, $C_{12} = 92$ GPa, $C_{13} = 71$ GPa, $C_{33} = 604$ GPa, $C_{44} = 116$ GPa and $C_{66} = 14$ GPa, respectively. The requirements for mechanical stability derived from the Born–Huang elastic stability criteria[28–30] in tetragonal systems are shown in eqn (1). T48-carbon satisfies them fully, indicating the mechanical stability of this structure.

$$C_{11} > |C_{12}|, 2C_{13}^{2} < C_{33}\left(C_{11}+C_{12}\right), C_{44} > 0, C_{66} > 0 \tag{1}$$

To study the energetic stability of T48-carbon, we carry out the calculation of total energy as a function of volume, as shown in Fig. 2(a). Through comparing the energy-volume curves of T48-carbon, graphite, diamond and some other theoretically predicted stable 3D carbon structures like H-6,[31] Tri-C9,[32] and K6,[33] one can see that although T48-carbon is less stable in energy than graphite and diamond, it is comparable to T6-carbon[1] and has more favorable energy over these theoretically predicted carbon allotropes, implying potential possibility for the experimental synthesis of T48-carbon.

3.2 Mechanical properties

Based on the calculated elastic stiffness matrix containing six independent nonzero components, we can study the mechanical properties. According to the Voigt–Reuss–Hill method,[34,35] we can evaluate the bulk modulus *B* and shear modulus *G* using the following equations [eqn (2)–(9)].

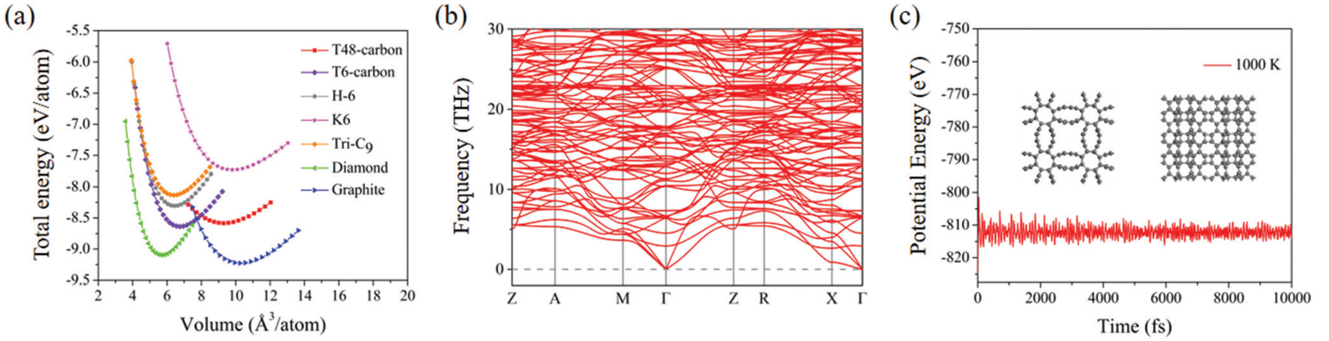

Fig. 2 (a) Variation of the total energy per atom for T48-carbon and some other carbon allotropes as a function of volume. (b) Phonon band structure and (c) total potential energy fluctuation during AIMD simulation at 1000 K. Insets show the snapshots of the geometry of T48-carbon at the end of the simulation.

$$M = C_{11} + C_{12} + 2C_{33} - 4C_{13} \tag{2}$$

$$C^2 = (C_{11} + C_{12})C_{33} - 2{C_{13}}^2 \tag{3}$$

$$G_V = (M + 3C_{11} - 3C_{12} + 12C_{44} + 6C_{66})/30 \tag{4}$$

$$G_R = 15/[(18B_V)/C^2 + 6/(C_{11} - C_{12}) + 6/C_{44} + 3/C_{66}] \tag{5}$$

$$B_V = [2(C_{11} + C_{12}) + C_{33} + 4C_{13}]/9 \tag{6}$$

$$B_R = C^2/M \tag{7}$$

$$G_H = \frac{1}{2}(G_R + G_V) \tag{8}$$

$$B_H = \frac{1}{2}(B_R + B_V) \tag{9}$$

$$E = \frac{9G_H B_H}{G_H + 3B_H} \tag{10}$$

$$\nu = \frac{3B_H - E}{6B_H} \tag{11}$$

The Voigt bound is the upper limit of the actual effective moduli when deformation is applied to the structure, while the Reuss bound is the lower limit. Thus, the Voigt–Reuss–Hill approximations, as the arithmetic average of Voigt and Reuss bounds, give reasonable descriptions to the actual effective moduli.[36] The calculated results are presented in Table 1. We can further evaluate the intrinsic ductility and brittleness[37,38] using the Poisson's ratio ν [see eqn (10) and (11)] and the ratio of G to B. Based on the results in Table 1, we can conclude that T48-carbon is ductile because it meets the requirements of $\nu > 0.26$ and $G/B < 0.57$, implying that T48-carbon is easy to deform reversely.

To explore the elastic anisotropy, we use the universal elastic anisotropy index A^U, percent compressible anisotropy A_{comp} and percent shear anisotropy A_{shear}.[39]

$$A^U = 5\frac{G_V}{G_R} + \frac{B_V}{B_R} - 6 \tag{12}$$

$$A_{\text{comp}} = \frac{B_V - B_R}{B_V + B_R} \times 100\% \tag{13}$$

$$A_{\text{shear}} = \frac{G_V - G_R}{G_V + G_R} \times 100\% \tag{14}$$

In addition, the shear anisotropic factors[40] should also be included to better investigate the mechanical anisotropy. They describe the response to shear force of different crystal planes, and A_1, A_2 and A_3 correspond to the (100), (010) and (001) planes, respectively.

$$A_1 = \frac{4C_{44}}{C_{11} + C_{33} - 2C_{13}} \tag{15}$$

$$A_2 = \frac{4C_{55}}{C_{22} + C_{33} - 2C_{23}} \tag{16}$$

$$A_3 = \frac{4C_{66}}{C_{11} + C_{22} - 2C_{12}} \tag{17}$$

For elastically isotropic materials, $A^U = A_{\text{comp}} = A_{\text{shear}} = 0$ and $A_1 = A_2 = A_3 = 1$, while larger A^U, A_{comp} and A_{shear} represent a higher elastic anisotropy for crystals.[41] The values of the elastic anisotropic indexes mentioned above are listed in Table 2. The A^U value (6.66) of T48-carbon is much larger than those of diamond (0.044)[42] and $I\bar{4}$-carbon (1.07),[43] implying a strong mechanical anisotropy. By comparing the values of A_{comp} (3.76%) and A_{shear} (39.68%), one can see that the shear anisotropy plays a dominant role in the universal anisotropy. The value of A_2 equals to that of A_1 (0.611) and is closer to unity

Table 1 Shear modulus G (in GPa), bulk modulus B (in GPa), Poisson's ratio ν, and Pugh's modulus ratio G/B of T48-carbon

Structure	G_V	G_R	B_V	B_R	G_H	B_H	ν	G/B
T48-carbon	114.1	49.27	186.02	172.54	81.69	179.28	0.30	0.46

Table 2 Universal elastic anisotropy index A^U, percent compressible anisotropy A_{comp}, percent shear anisotropy A_{shear}, shear anisotropic factors A_1, A_2 and A_3 and Young's modulus E (in GPa) along different directions

Structure	A^U	A_{comp}	A_{shear}	A_1	A_2	A_3	E_x	E_y	E_z
T48-carbon	6.66	3.76%	39.68%	0.611	0.611	0.138	268.1	268.1	578.0

than A_3's value (0.138), implying that the anisotropy in the (001) plane is higher than those in the (100) and (010) planes.

From the elastic stiffness tensor, we can conclude the elastic compliance matrix of T48-carbon. By using the following equation, we can investigate the elastic anisotropy of Young's modulus E.[44]

$$\begin{aligned}\frac{1}{E} = {} & S_{11}(l_1^4 + l_2^4) + (2S_{13} + S_{44})(l_1^2 l_3^2 + l_2^2 l_3^2) \\ & + S_{33} l_3^4 + (2S_{12} + S_{66}) l_1^2 l_2^2\end{aligned} \tag{18}$$

Here, S_{ij} are the usual elastic compliance constants. l_1, l_2 and l_3 are the direction cosines. The resulting Young's modulus E along the x-, y- and z-directions are 268.1, 268.1 and 578.0 GPa, respectively. This is consistent with the elastic constants in the elastic stiffness tensor that C_{33} is much larger than C_{11} and C_{22}.

We also calculated the maximum tensile strength of T48-carbon. By applying the quasi-static displacement-controlled deformation with every 1% strain intervals along x-, y- and z-directions, we can obtain the stress–strain curves of T48-carbon as shown in Fig. 3. T48-carbon exhibits a nearly linear stress–strain response along the x- and y-directions with the maximum tensile strain and tensile stress of 11% and 25.6 GPa, respectively. While the stress–strain curve in the z-direction shows two opposite tendencies. It increases in a nearly straight-line trend first and then decreases at larger strain, the corresponding maximum tensile strain and maximum tensile stress are 19% and 73.4 GPa, respectively. For comparison, one can find that the ideal tensile strength of T48-carbon along the z-direction shows a larger value than other directions and exhibits better performance than those in the z-direction of penta-h22[45] and Hex-C_{558}[3] obviously.

3.3 Electronic properties

To study the electronic properties of T48-carbon, we first calculated its electronic band structure and partial density of states (PDOS). As shown in Fig. 4(a), partially occupied energy bands cross the Fermi level at both the PBE and HSE06 levels, suggesting that T48-carbon is metallic. T48-carbon inherits the metallicity of biphenylene, as is the case with HZGM-42 that inherits the semi-metallic feature of graphene. Furthermore, we calculated the electron localization function (ELF) to identify the electron conducting channels in T48-carbon. The ELF can describe the localization of electrons in the range of 0.0–1.0, where 0.0 corresponds to a very low charge density of electrons, 1.0 corresponds to a region of fully localized electrons and 0.5 corresponds to the completely delocalized electrons. From the ELFs of (110) and (100) slices in Fig. 4(b), one can see the electronic conducting channels (green channels) in the red rectangle regions obviously, further confirming the metallicity of T48-carbon.

3.4 Origin of metallicity

To investigate the origin of metallicity in T48-carbon, we analyzed the results of PDOS, as shown in Fig. 4(a), to decompose the contributions from different carbon atoms and orbitals to the electronic energy bands. One can see that the density of states at the Fermi level is mainly contributed from the p-orbital of sp^2-hybridized C_2 and C_3 atoms. This can be understood by checking the geometry of T48-carbon, where C_1 atoms are four-fold coordinated carbon atoms with sp^3-hybridized bondings, forming new covalent bonds to link the nanoribbons together, so the valence electrons of C_1 atoms are localized. While C_2 and C_3 atoms, due to the in-plane structural feature of biphenylene nanoribbons, are

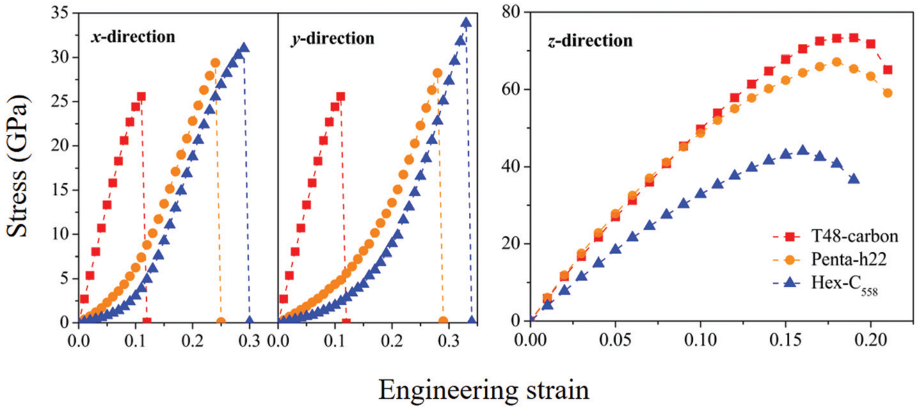

Fig. 3 The stress–strain relationships of the tensile deformations in the x-, y-, and z-directions for T48-carbon, penta-h22, and Hex-C_{558}.

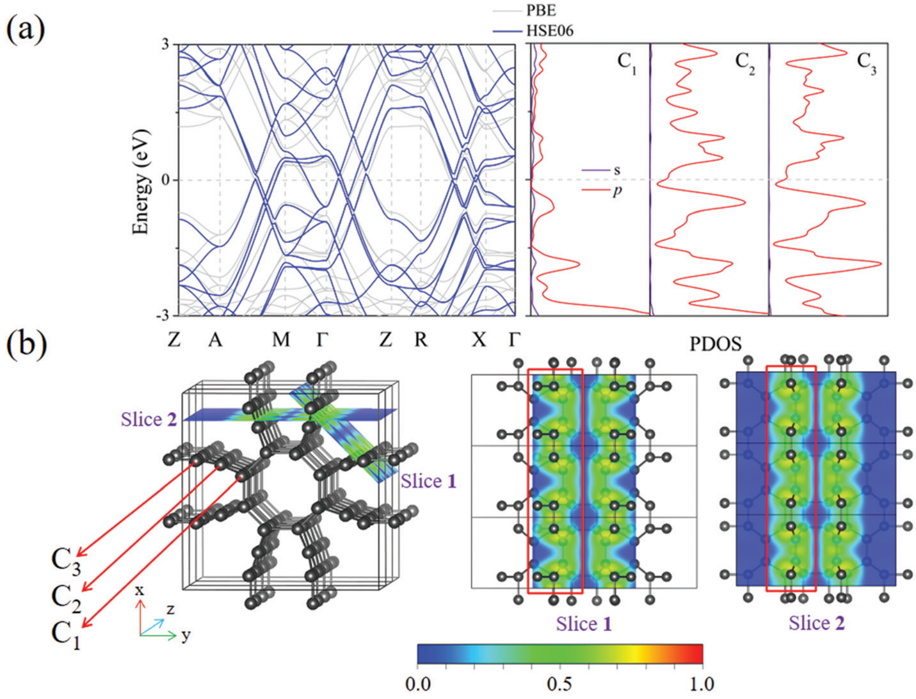

Fig. 4 (a) Electronic band structure at the PBE and HSE06 levels and PDOS at the HSE06 level of T48-carbon. (b) ELF distribution of two slices on shifted lattice planes (110) and (100).

three-fold coordinated with sp^2 hybridization. The remaining p-orbitals overlap with each other and form a large π-conjugated system similar to that in graphene, in which π electrons are highly delocalized. This is consistent with other theoretically proposed metallic 3D carbon structures such as T6- and T14-carbon that sp^3-bonded carbon atoms guarantee the stability and sp^2 bonded carbon atoms ensure the metallicity.[1]

To clearly see the distributions and interactions of the dumbbell-shaped p-orbital of sp^2-hybridized C_3 and C_2 atoms, we calculated the band-decomposed charge densities of T48-carbon. We focus on π(C_3–C_3), π(C_2–C_2) and π(C_3–C_2) bonds, as the pink, purple and orange slices shown in Fig. 5(a). For T48-carbon, there are 96 pairs of valence electrons in each unit cell. Therefore, we selected six energy bands whose order number is 94 to 99 ranging from −3 eV to +3 eV in the vicinity

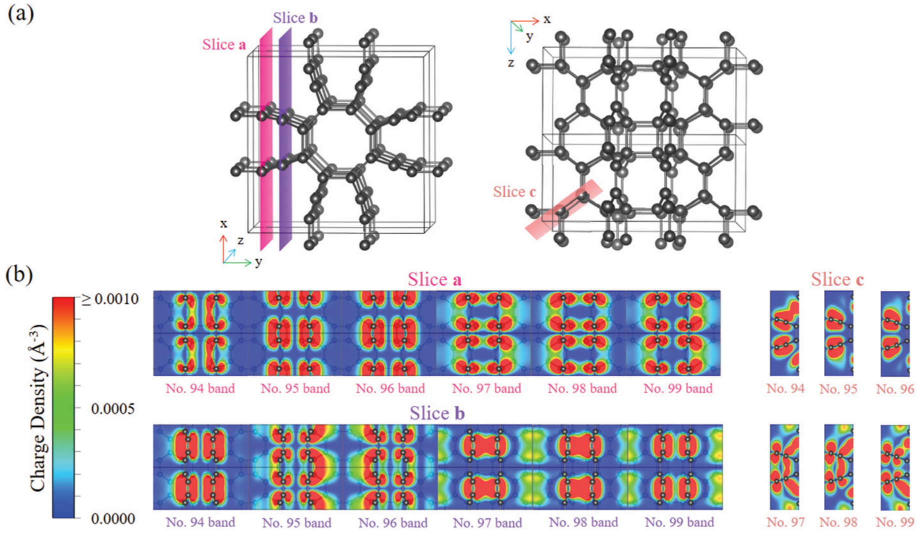

Fig. 5 (a) Selected slices for the investigation of π(C_3–C_3), π(C_2–C_2) and π(C_3–C_2) bonds. (b) Band-decomposed charge density of no. 94-99 energy bands within the range of −3 eV–3 eV.

Table 3 Comparison of T48-carbon with some other theoretically predicted carbon monoliths

Materials	Structural units	Electronic properties	Mechanical properties	Mass density (g cm^{-3})	Specific heat capacity [J (K mol)$^{-1}$]	Origin of metallicity
T48-carbon	Biphenylene	Metallic	Ductile	2.15	8.99	p$_z$-Orbital of sp^2-hybridized carbon atoms
HZGM-42 [46]	Graphene	Semimetallic	Brittle	1.39	8.47	
Penta-oC36 [4]	Penta-graphene	Metallic	Ductile	1.41	9.08	
Hex-C$_{558}$ [3]	OP graphene-Z	Metallic	Ductile	1.05	9.15	
3D-(4,0) carbon[47]	(4,0) carbon nanotubes	Metallic	Ductile	3.31	7.86	

of the Fermi level. One can see that the charge density all localized around C$_3$ and C$_2$ atoms. We found that the charge density of π(C$_3$–C$_3$) and π(C$_2$–C$_2$) bonds overlaps with their periodic images in the *z*-direction, confirming the metallic channel along that direction. Thus, we conclude that the metallicity of T48-carbon mainly originates from the p$_z$-orbitals of the sp^2-hybridized C$_3$ and C$_2$ carbon atoms. Besides, the energy level inversions appear near the Fermi level, where electron states with antibonding features are lower in energy than those with bonding features. For example, the charge density with antibonding features is found in band no. 94 on π(C$_3$–C$_3$) (see slice a) and bands no. 95-96 on π(C$_2$–C$_2$) (see slice b), which all appear below the Fermi level. This is because they are conjugated with the bonding orbital of π(C$_3$–C$_2$) (see slice c).

For clarity, we summarized the basic structural information and physical properties of some similar carbon allotropes in Table 3. One can see that T48-carbon, as a 3D metallic and ductile carbon monolith based on biphenylene nanoribbons, has a moderate mass density and a relatively high specific heat capacity.

4. Conclusions

In summary, based on first-principles calculations, we propose a new porous 3D metallic carbon structure named T48-carbon by assembling the nanoribbons of experimentally synthesized 2D biphenylene. T48-carbon is not only dynamically, thermally and mechanically stable, but also more favorable in energy compared with some other theoretically predicted carbon allotropes. T48-carbon is mechanically anisotropic and shear anisotropy plays a dominant role, and is ductile with its maximum engineering strain of 19% and maximum tensile strength of 73.4 GPa along the *z*-direction. Furthermore, T48-carbon inherits the metallicity of biphenylene, which mainly originates from the p$_z$-orbital of sp^2-hybridized carbon atoms. Compared with some other carbon allotropes, T48-carbon has a moderate mass density (2.15 g cm^{-3}) and a relatively high specific heat capacity [8.99 J (K mol)$^{-1}$]. This work shows that the diversity of 3D metallic carbon can be built from various experimentally synthesized carbon sheets, expanding the family of 3D metallic carbon.

Conflicts of interest

There are no conflicts to declare.

Acknowledgements

This work was partially supported by grants from the National Key Research and Development Program of the Ministry of Science and Technology of China (Grant No. 2017YFA0205003) and the National Natural Science Foundation of China (Grants No. NSFC-11974028 and NSFC-21773004). It is also supported by the high-performance computing platform of Peking university, China.

References

1 S. Zhang, Q. Wang, X. Chen and P. Jena, *Proc. Natl. Acad. Sci. U. S. A.*, 2013, **110**, 18809.
2 J. Liu, T. Zhao, S. Zhang and Q. Wang, *Nano Energy*, 2017, **38**, 263–270.
3 D. Ni, Y. Shen, Y. Shen, Q. Wang, Y. Kawazoe and P. Jena, *Carbon*, 2021, **183**, 652–659.
4 S. Li, Y. Shen, D. Ni and Q. Wang, *J. Mater. Chem. A*, 2021, **9**, 23214–23222.
5 Q. Fan, L. Yan, M. W. Tripp, O. Krejčí, S. Dimosthenous, S. R. Kachel, M. Chen, A. S. Foster, U. Koert, P. Liljeroth and J. M. Gottfried, *Science*, 2021, **372**, 852–856.
6 N. N. Karaush, G. V. Baryshnikov and B. F. Minaev, *Chem. Phys. Lett.*, 2014, **612**, 229–233.
7 Y. Luo, C. Ren, Y. Xu, J. Yu, S. Wang and M. Sun, *Sci. Rep.*, 2021, **11**, 19008.
8 M. A. Hudspeth, B. W. Whitman, V. Barone and J. E. Peralta, *ACS Nano*, 2010, **4**, 4565–4570.
9 N. N. Karaush, S. V. Bondarchuk, G. V. Baryshnikov, V. A. Minaeva, W. Sun and B. F. Minaev, *RSC Adv.*, 2016, **6**, 49505.
10 Y.-B. Ma, T. Ouyang, Y.-P. Chen and Y.-E. Xie, *Chin. Phys. B*, 2021, **30**, 077103.
11 D. Ferguson, D. J. Searles and M. Hankel, *ACS Appl. Mater. Interfaces*, 2017, **9**, 20577–20584.
12 M. M. Obeid and Q. Sun, *Carbon*, 2022, **188**, 95–103.
13 G. Kresse and J. Furthmüller, *Phys. Rev. B: Condens. Matter Mater. Phys.*, 1996, **54**, 11169–11186.
14 P. E. Blöchl, *Phys. Rev. B: Condens. Matter Mater. Phys.*, 1994, **50**, 17953–17979.
15 G. Kresse and D. Joubert, *Phys. Rev. B: Condens. Matter Mater. Phys.*, 1999, **59**, 1758–1775.
16 J. P. Perdew, K. Burke and M. Ernzerhof, *Phys. Rev. Lett.*, 1996, **77**, 3865–3868.

17 J. Heyd, G. E. Scuseria and M. Ernzerhof, *J. Chem. Phys.*, 2003, **118**, 8207–8215.

18 H. J. S. Ge and M. Ernzerhof, *J. Chem. Phys.*, 2006, **124**, 219906.

19 H. J. Monkhorst and J. D. Pack, *Phys. Rev. B: Solid State*, 1976, **13**, 5188–5192.

20 K. Parlinski, Z. Q. Li and Y. Kawazoe, *Phys. Rev. Lett.*, 1997, **78**, 4063–4066.

21 A. Togo and I. Tanaka, *Scr. Mater.*, 2015, **108**, 1–5.

22 D. Bucher, L. C. T. Pierce, J. A. McCammon and P. R. L. Markwick, *J. Chem. Theory Comput.*, 2011, **7**, 890–897.

23 D. J. Evans and B. L. Holian, *J. Chem. Phys.*, 1985, **83**, 4069–4074.

24 K. Kim, T. Lee, Y. Kwon, Y. Seo, J. Song, J. K. Park, H. Lee, J. Y. Park, H. Ihee, S. J. Cho and R. Ryoo, *Nature*, 2016, **535**, 131–135.

25 N. V. Krainyukova and E. N. Zubarev, *Phys. Rev. Lett.*, 2016, **116**, 055501.

26 D. Li, F. Tian, B. Chu, D. Duan, S. Wei, Y. Lv, H. Zhang, L. Wang, N. Lu and B. Liu, *J. Mater. Chem. A*, 2015, **3**, 10448–10452.

27 Y. Le Page and P. Saxe, *Phys. Rev. B: Condens. Matter Mater. Phys.*, 2002, **65**, 104104.

28 M. Born, K. Huang and M. Lax, *Am. J. Physiol.*, 1955, **23**, 474–474.

29 Y. Ding and Y. Wang, *J. Phys. Chem. C*, 2013, **117**, 18266–18278.

30 F. Mouhat and F.-X. Coudert, *Phys. Rev. B: Condens. Matter Mater. Phys.*, 2014, **90**, 224104.

31 Z. G. Fthenakis, *RSC Adv.*, 2016, **6**, 78187–78193.

32 Y. Cheng, R. Melnik, Y. Kawazoe and B. Wen, *Cryst. Growth Des.*, 2016, **16**, 1360–1365.

33 C.-Y. Niu, X.-Q. Wang and J.-T. Wang, *J. Chem. Phys.*, 2014, **140**, 054514.

34 R. Hill, *Proc. Phys. Soc., London, Sect. A*, 1952, **65**, 349–354.

35 R. Li and Y. Duan, *Philos. Mag.*, 2016, **96**, 972–990.

36 Z.-j. Wu, E.-j. Zhao, H.-p. Xiang, X.-f. Hao, X.-j. Liu and J. Meng, *Phys. Rev. B: Condens. Matter Mater. Phys.*, 2007, **76**, 054115.

37 S. F. Pugh, *London, Edinburgh Dublin Philos. Mag. J. Sci.*, 1954, **45**, 823–843.

38 B. Huang, Y.-H. Duan, Y. Sun, M.-J. Peng and S. Chen, *J. Alloys Compd.*, 2015, **635**, 213–224.

39 S. I. Ranganathan and M. Ostoja-Starzewski, *Phys. Rev. Lett.*, 2008, **101**, 055504.

40 P. Ravindran, L. Fast, P. A. Korzhavyi, B. Johansson, J. Wills and O. Eriksson, *J. Appl. Phys.*, 1998, **84**, 4891–4904.

41 D. H. Chung and W. R. Buessem, *J. Appl. Phys.*, 1967, **38**, 2010–2012.

42 Y. Zhou, X. Chen, S.-L. Liu and L.-H. Gan, *Solid State Commun.*, 2021, **323**, 114095.

43 M. Xing, B. Li, Z. Yu and Q. Chen, *Materials*, 2016, **9**, 484.

44 Y. H. Duan, Y. Sun and M. J. Peng, *Comput. Mater. Sci.*, 2014, **92**, 258–266.

45 D. Ni, Y. Guo, Y. Shen and Q. Wang, *Adv. Theory Simul.*, 2021, **4**, 2100025.

46 J. Liu, X. Li, Q. Wang, Y. Kawazoe and P. Jena, *J. Mater. Chem. A*, 2018, **6**, 13816–13824.

47 Z. Zhao, B. Xu, L.-M. Wang, X.-F. Zhou, J. He, Z. Liu, H.-T. Wang and Y. Tian, *ACS Nano*, 2011, **5**, 7226–7234.